

Fast Lidar and Radar Multiple-Scattering Models. Part I: Small-Angle Scattering Using the Photon Variance–Covariance Method

ROBIN J. HOGAN

Department of Meteorology, University of Reading, Reading, United Kingdom

(Manuscript received 5 October 2007, in final form 7 April 2008)

ABSTRACT

A fast, approximate method is described for the calculation of the intensity of multiply scattered lidar returns from clouds. At each range gate it characterizes the outgoing photon distribution by its spatial variance, the variance of photon direction, and the covariance of photon direction and position. The result is that for an N -point profile the calculation is $O(N)$ efficient yet it implicitly includes all orders of scattering, in contrast with the $O(N^m/m!)$ efficiency of models that explicitly consider each scattering order separately for truncation at m -order scattering. It is also shown how the shape of the scattering phase function near 180° may be taken into account for both liquid water droplets and ice particles. The model considers only multiple scattering due to small-angle forward-scattering events, which is suitable for most ground-based and airborne lidars because of their small footprint on the cloud. For spaceborne lidar, it must be used in combination with the wide-angle multiple scattering model described in Part II of this two-part paper.

1. Introduction

Lidar and radar have been used extensively from the ground to study clouds (Ackerman and Stokes 2003; Illingworth et al. 2007), but from space (Stephens et al. 2002; Winker et al. 2003) the interpretation of the back-scattered signals is made more complicated by the much larger instrument footprints, which result in a greater fraction of the detected photons having undergone multiple scattering. It was shown by Hogan et al. (2006) that if consideration of lidar multiple-scattering effects is omitted in combined radar–lidar retrievals of ice clouds from space, the retrieved optical depth will be underestimated by around 40%. This two-part paper presents a new method for modeling such returns that is fast enough to be incorporated as a forward model in cloud retrieval schemes (e.g., Donovan et al. 2001; Tinel et al. 2005; Delanoë and Hogan 2008).

By way of an introduction to the problem of multiple scattering, we consider the four scattering regimes that may be experienced by active remote sensors; a similar

taxonomy was provided by Nicolas et al. (1997) but only for lidar. The regimes are shown schematically in Fig. 1 and are as follows:

Regime 0: No attenuation. The trivial case occurs when the optical depth of a medium $\delta \ll 1$ and the apparent backscatter $\hat{\beta}$ (or in the case of radar, the apparent radar reflectivity factor \hat{Z}) is equal to the “true” backscatter of the medium β (or Z) and can be interpreted unambiguously. This is the case for lidar observations of thin aerosol layers, millimeter-wave radar observations of ice clouds and centimeter-wave radar observations of light to moderate rain.

Regime 1: Single scattering. In an optically thicker medium, provided that any scattered photons leave the field of view of the receiver and are not detected (except those in the exact backscatter direction), the apparent backscatter measured at a range r is given simply by

$$\hat{\beta}(r) = \beta(r) \exp[-2\delta(r)], \quad (1)$$

where $\delta(r)$ is the optical depth of clouds, aerosols, and gases between the instrument and r . Such conditions are experienced by a ground-based lidar observing an optically thick aerosol layer, a mm-

Corresponding author address: Robin J. Hogan, Department of Meteorology, University of Reading, Earley Gate, P.O. Box 243, Reading RG6 6BB, United Kingdom.
E-mail: r.j.hogan@reading.ac.uk

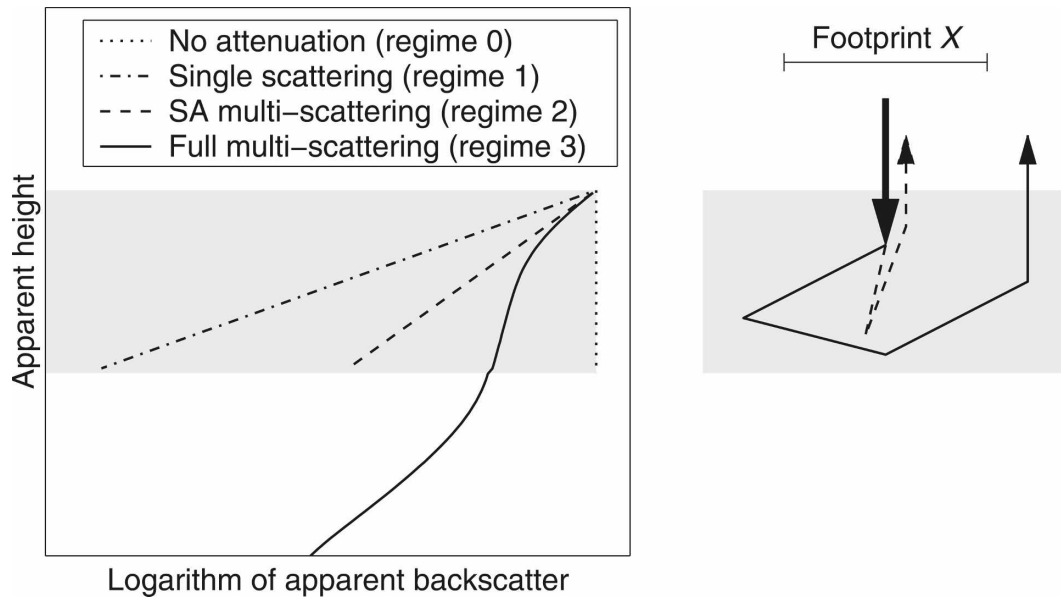


FIG. 1. Depiction of the four scattering regimes that active sensors encounter, as discussed in the text. The axes on the left indicate the apparent backscatter that a nadir-looking instrument would observe in a homogeneous slab of cloud in each of the four regimes. The schematic on the right depicts the nadir beam entering the cloud (thick arrow), with the dashed arrow showing the trajectory of a photon subject to a small-angle (SA) forward-scattering event on both the outgoing and return journey but only one large-angle scattering event. The thin solid arrow shows the trajectory of a photon subject to wide-angle scattering before being returned to the receiver; in this regime, the extra path length leads to the photon appearing to have originated below the cloud. The relevant regime is determined by whether such returned photons typically lie within or outside the receiver footprint.

wave radar observing liquid clouds, and a cm-wave radar observing heavy rain.

Regime 2: Small-angle multiple scattering. In the case of lidar, where cloud particles are typically much larger than the wavelength, Babinet's principle states that half of the extinguished energy is scattered into a narrow forward lobe of $1/e$ half-width $\Theta = \lambda/(\pi a)$, where λ is the wavelength and a is the radius of the particle (van de Hulst 1957; Hogan 2006, hereafter H06). For typical ground-based lidar observations of ice and liquid clouds and spaceborne lidar observations of ice clouds and aerosols, the field of view is such that these small-angle forward-scattered photons may remain within the field of view of the detector and contribute to the apparent backscatter, whereas photons that experience wide-angle scattering will typically be transported outside the field of view such that they are not detected. Because the distance traveled by photons that have only undergone small-angle scattering is approximately the same as unscattered photons, the time of travel can still be converted unambiguously into the distance of the target from the instrument, even though the intensity is more difficult to interpret. The condition for this behavior to occur is

$$l_s \Theta \lesssim X \ll l_t, \quad (2)$$

where X is the width of the "footprint" projected by the field of view of the receiver at the range of the target, $l_s = 1/\alpha_s$ is the scattering mean-free path, α_s is the scattering coefficient, $l_t = l_s/(1 - \tilde{\omega}g)$ is the transport mean-free-path, $\tilde{\omega}$ is the single scattering albedo, and g is the asymmetry factor defined as the average cosine of the scattering phase function: $g = \langle \cos\theta \rangle$.

Regime 3: Wide-angle multiple scattering. When X is on the same order as or larger than l_t , then wide-angle scattered photons may remain within the field of view and be detected, but with a time delay that makes them appear to have originated at a range beyond the distance to which they actually penetrated. This "pulse stretching" is illustrated in Fig. 1 and is particularly visible in spaceborne lidar observations of liquid water clouds (Platt and Winker 1995), but it is also apparent in observations by the *CloudSat* 94-GHz radar in deep tropical convective precipitation (Battaglia et al. 2007).

Part I of this two-part paper presents a very fast method for calculating small-angle multiple scattering (regime 2 above), which is suited for application on its own to ground-based lidar. Part II (Hogan and Batta-

glia 2008, hereafter Part II) then presents a method to model wide-angle multiple scattering (regime 3 above) using the time-dependent two-stream approximation. Even in regime 3, the apparent backscatter in the first few optical depths of penetration into the medium are dominated by scattering in regimes 1 (for radar) or 2 (for lidar), requiring a hybrid approach. This is described fully in Part II.

There is extensive literature on methods to model small-angle multiple scattering [sometimes referred to as “quasi-small-angle;” e.g., Bissonnette (2005)]. The simplest method was proposed by Platt (1973), who introduced a term η into (1) to obtain

$$\hat{\beta}^d(r) = \beta(r) \exp[-2\eta\delta(r)], \quad (3)$$

where the superscript d is used to distinguish between this “quasi-direct” return and the return due to wide-angle scattering in Part II. The value of η can vary between 1 (the single-scattering limit) and 1/2 (the wide field-of-view limit). The latter case corresponds to all the photons in the forward lobe remaining within the receiver field of view; thus, η has the effect of reducing the effective optical depth such that these photons are treated as if they had not been scattered at all. If the medium is represented by an N -point profile of extinction values, then the calculation of (3) is $O(N)$ efficient. However, the problem with this approach is that forward-scattered photons progressively escape from the field of view with increasing distance downstream of the scattering event, implying that η should increase with range. Unfortunately, there is no satisfactory theory for deriving η and its range dependence for a particular lidar geometry and scattering phase function.

Eloranta (1998, hereafter E98) took a more rigorous approach, explicitly calculating each scattering order separately. His algorithm achieved $O(N^m/m!)$ efficiency when considering up to m orders of scattering. H06 used Eloranta’s approach for double scattering, but treated all orders of scattering above the second order together in such a way that the whole algorithm was $O(N^2)$ efficient. This was achieved by modeling the variance and covariance of photon position and direction. It was found to be typically as accurate as Eloranta’s algorithm taken to the fifth order, but much more efficient.

In section 2 of this paper it is shown that the H06 method can be regarded as one of a family of “photon variance–covariance” (PVC) methods, a new example of which is then presented that achieves $O(N)$ efficiency with only a small reduction in accuracy compared to H06. In section 3, the extra calculations necessary to account for anisotropic scattering in the near-

180° direction by liquid water droplets and ice particles are described. This is followed by comparisons with existing methods for small-angle multiple scattering in section 4. A fast approximate method to estimate the Jacobian is then presented in section 5, which is necessary if this method is to be used as the forward model in a variational retrieval scheme (e.g., Delanoë and Hogan 2008).

2. Method

a. Introductory considerations

The main scatterers that are important for lidar are cloud particles, aerosols, and molecules. We denote the combined extinction coefficient of all scatterers and absorbers versus range as $\alpha(r)$. However, only cloud particles are sufficiently large compared to the wavelength to produce a narrow forward lobe in the phase function. Because in Part I we are only concerned with small-angle multiple scattering, we introduce the “large-particle extinction coefficient” $\alpha^c(r)$ to represent the extinction that is caused only by cloud particles. It should be noted that the optical depth in (1) is defined in terms of the total extinction: $\delta(r) = \int_0^r \alpha(r) dr$. The scattering by aerosols and molecules (and the component of scattering by cloud particles that is not in the forward lobe) can still contribute to multiple scattering, but only in the wide-angle regime addressed in Part II. Note that for radar, even the largest precipitation particles are too small to produce a significant forward lobe, so any multiple scattering will be in the wide-angle regime.

The formulation of the algorithm is simplified by the use of the “equivalent-medium theorem,” which has been proved to be valid under the small-angle approximation (Katsev et al. 1997; Bissonnette 2005). This theorem states that the backscatter measured in a medium is the same as that from an equivalent hypothetical medium that has twice the extinction and scattering coefficients (but the same phase function) as the true medium on the outward journey but zero extinction and scattering on the return journey. Thus, the two-way problem is transformed into a simpler one-way propagation problem.

The following assumptions are made in common with E98 and H06: (i) both the laser divergence and the forward-scattering lobe from a distribution of particles may be represented as Gaussians, (ii) the extra path length of multiply scattered photons may be neglected, (iii) the lidar is monostatic so that the problem has azimuthal symmetry, and (iv) all angles are small enough that $\sin\theta \approx \theta$.

b. Calculation of the energy and variance of the outgoing photon distribution

Using nomenclature similar to that in H06, we consider a laser transmitter that emits a short pulse of total energy P_0 in a Gaussian beam with a $1/e$ angular half-width of ρ_{tr} . At a distance r from the instrument, the energy density of outgoing unscattered photons (in units of J m^{-2}) in the equivalent medium is a function of r and of s , the distance perpendicular to the laser axis:

$$E_u(r, s) = \frac{P_u(r)}{\pi \overline{s_u^2}(r)} \exp\left[-\frac{s^2}{\overline{s_u^2}(r)}\right], \quad (4)$$

where the variance of the lateral distance of the unscattered photons to the lidar axis is

$$\overline{s_u^2}(r) = \rho_{tr}^2 r^2, \quad (5)$$

and the total unscattered energy reaching range r is $P_u(r) = P_0 \exp[-2\delta(r)]$. Note that the factor of 2 in the exponent is due to the doubled optical depth of the equivalent medium.

The main task of the algorithm is to estimate the distribution of forward-scattered photons as a function of r and s . It is convenient to treat the forward-scattered photon distribution as the sum of several separate distributions (E_a , E_b , etc.), such that the ‘‘combined’’ distribution (unscattered plus forward scattered) is given by

$$E(r, s) = E_u(r, s) + E_a(r, s) + E_b(r, s) + \dots, \quad (6)$$

from which the apparent backscatter may be calculated (section 2d). In the case of the H06 algorithm, E_a would represent photons forward scattered only a single time (i.e., those that contribute to double scattering), whereas E_b would represent photons forward scattered multiple times, and there would be no further terms in (6). These distributions can be characterized by their total energies (P , P_a , etc.) and spatial variances ($\overline{s^2}$, $\overline{s_a^2}$, etc.), which are functions of r alone. It is convenient to normalize the energies by the energy in the unscattered beam such that $\hat{P} = P/P_u$ and similarly for \hat{P}_a , etc. The normalized energies and the variances then satisfy

$$\hat{P} = 1 + \hat{P}_a + \hat{P}_b + \dots; \quad (7)$$

$$\hat{P}\overline{s^2} = \overline{s_u^2} + \hat{P}_a\overline{s_a^2} + \hat{P}_b\overline{s_b^2} + \dots. \quad (8)$$

It turns out that the easiest way to calculate the variables describing the forward-scattered distributions is to first calculate the corresponding variables for the full distribution, $\hat{P}(r)$ and $\overline{s^2}(r)$. Note that these variables have exact definitions even though it is not implied that

the full distribution has a particular form (such as Gaussian). The normalized total energy of the combined distribution is given by

$$\hat{P}(r) = \exp\left[\int_0^r \alpha^c(r') dr'\right], \quad (9)$$

which expresses the fact that forward scattering by cloud particles has the effect of reducing the effective extinction by a factor $\alpha^c/2$, leading to \hat{P} increasing with range. The use of the equivalent medium theorem leads to a doubling of the $\alpha^c/2$ factor when used in (9).

The bulk of this section is concerned with how to calculate $\overline{s^2}(r)$ exactly, subject to the assumptions given at the end of section 2a. To do this with $O(N)$ efficiency, it is necessary to keep track of two other variables: the variance of photon direction $\overline{\zeta^2}(r)$ and a variable representing the covariance of photon position and direction,¹ $C^{s\zeta}(r)$. We require differential equations to express how these variables vary with range. Consider first the spatial variance, which is the sum of the variances in the two orthogonal directions: $\overline{s^2} = \overline{x^2} + \overline{y^2}$. Figure 2 shows that if a photon travels away from the lidar a short distance dr then its lateral distance in the x direction changes by

$$dx = \zeta_x dr. \quad (10)$$

Hence,

$$dx^2 = 2x dx = 2x \zeta_x dr. \quad (11)$$

Taking the mean over all outgoing photons yields $d\overline{x^2} = 2\overline{x\zeta_x} dr$. By defining $C^{s\zeta} = \overline{x\zeta_x} + \overline{y\zeta_y}$, we obtain

$$d\overline{s^2} = 2C^{s\zeta} dr. \quad (12)$$

Thus, the evolution of $\overline{s^2}$ depends on the evolution of the covariance term $C^{s\zeta}$. To calculate $C^{s\zeta}$, we first consider the evolution of $(x\zeta_x)$. By definition,

$$d(x\zeta_x) = \zeta_x dx + x d\zeta_x. \quad (13)$$

Substituting (10) into the first term on the right-hand side and averaging over all photons yields $d\overline{x\zeta_x} = \overline{\zeta_x^2} dr$. The second term on the right-hand side of (13) has disappeared in the averaging process because $d\zeta_x$ represents the change in propagation angle due to a scattering event, which is uncorrelated to the position x . The definition $\overline{\zeta^2} = \overline{\zeta_x^2} + \overline{\zeta_y^2}$ then yields

$$dC^{s\zeta} = \overline{\zeta^2} dr. \quad (14)$$

Thus, the evolution of $C^{s\zeta}$ depends on the evolution of $\overline{\zeta^2}$. The propagation angle of photons within the distri-

¹ Note that $C^{s\zeta}$ was written as $\overline{s\zeta}$ by H06, which is not strictly correct.

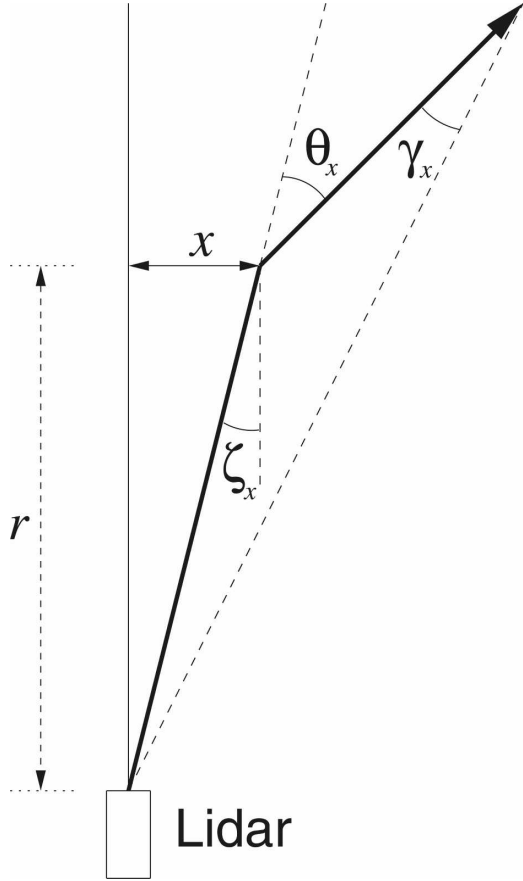


FIG. 2. Schematic of the trajectory of a single photon (thick line) in one of the two directions perpendicular to the lidar axis (thin vertical line). At range r the photon has a distance x from the lidar axis and an angle ζ_x with respect to it. It is then scattered by an angle θ_x . If it is subsequently scattered back toward the lidar, then the scattering coangle is denoted by γ_x . Note that the x axis has been exaggerated with respect to the r axis in this diagram because in practice all of these angles are small. The same diagram could be drawn in the r - y plane to define the variables y , ζ_y , θ_y , and γ_y .

bution under consideration is only changed by small-angle forward-scattering events because wide-angle scattered photons are lost from the distribution. As the distribution propagates through the medium, the effect of forward scattering is to increase the variance of the photon propagation angle. H06 showed that the standard deviation of the scattering angle may be defined as $\Theta = \lambda/(\pi a_G)$, where a_G is the equivalent-area radius of the size distribution such that $\pi a_G^2 = \langle G \rangle$, and $\langle G \rangle$ is the mean cross-sectional area of the scattering particles. Thus, the evolution of ζ^2 is governed by

$$d\zeta^2 = \alpha^c \Theta^2 dr. \tag{15}$$

Note that in this equation there has been a cancelation of the factor of 2 (which was due to the use of an

equivalent medium) by a factor of 1/2 (which was present because only half of the extinguished energy ends up in the forward lobe).

In practice, the variables α^c and Θ^2 are defined at discrete points in range, so it is necessary to numerically integrate (12), (14), and (15) forward together. It is assumed that the values at range gate i (α_i^c and Θ_i^2), are constant between the ranges $r_{i-1/2}$ and $r_{i+1/2}$. Before the photons have encountered any small-angle scatterers, the three variables ζ^2 , $C^{s\zeta}$, and s^2 are the same as for the unscattered distribution and are determined by the geometry of the instrument such that $\zeta^2 = \zeta_u^2 = \rho_{tr}^2$, $C^{s\zeta} = C_u^{s\zeta} = r\rho_{tr}^2$, and $s^2 = s_u^2 = r^2\rho_{tr}^2$ (H06). Given the values of these variables at half-gate $i - 1/2$, we may calculate them at half-gate $i + 1/2$ as follows. First we integrate (15) across the range gate to get

$$\overline{\zeta_{i+1/2}^2} = \overline{\zeta_{i-1/2}^2} + \alpha_i^c \Theta_i^2 \Delta r_i, \tag{16}$$

where $\Delta r_i = r_{i+1/2} - r_{i-1/2}$. Next, we substitute $\overline{\zeta^2} = \overline{\zeta_{i-1/2}^2} + \alpha_i^c \Theta_i^2 \times (r - r_{i-1/2})$ into (14) and integrate:

$$\begin{aligned} C_{i+1/2}^{s\zeta} &= C_{i-1/2}^{s\zeta} + \int_{r_{i-1/2}}^{r_{i+1/2}} \overline{\zeta^2} dr \\ &= C_{i-1/2}^{s\zeta} + \overline{\zeta_{i-1/2}^2} \Delta r_i + \alpha_i^c \Theta_i^2 \Delta r_i^2 / 2. \end{aligned} \tag{17}$$

Likewise, by integration of (12) we obtain

$$\begin{aligned} \overline{s_{i+1/2}^2} &= \overline{s_{i-1/2}^2} + 2C_{i-1/2}^{s\zeta} \Delta r_i \\ &\quad + \overline{\zeta_{i-1/2}^2} \Delta r_i^2 + \alpha_i^c \Theta_i^2 \Delta r_i^3 / 3. \end{aligned} \tag{18}$$

Because of modifications made to these variables in section 2c, it is necessary to define the “sequential” form of (9) as

$$\hat{P}_{i+1/2} = \hat{P}_{i-1/2} \exp(\alpha_i^c \Delta r). \tag{19}$$

Therefore, the sequential application of (16)–(19) allows \hat{P} , ζ^2 , $C^{s\zeta}$, and s^2 to be calculated at each half-gate.

The strength of this method is that arbitrary orders of scattering are represented without having to model each of them explicitly. The use of the differential Eq. (15) and its subsequent integration over a range gate in (16) even allows a photon to be scattered several times within a single range gate.

c. Estimation of the shape of the forward-scattered distribution

The previous subsection has shown how the energy and variance of the full photon distribution may be calculated exactly (subject to the assumptions at the end of section 2a). The simplest strategy for estimating the contribution of multiple scattering to apparent

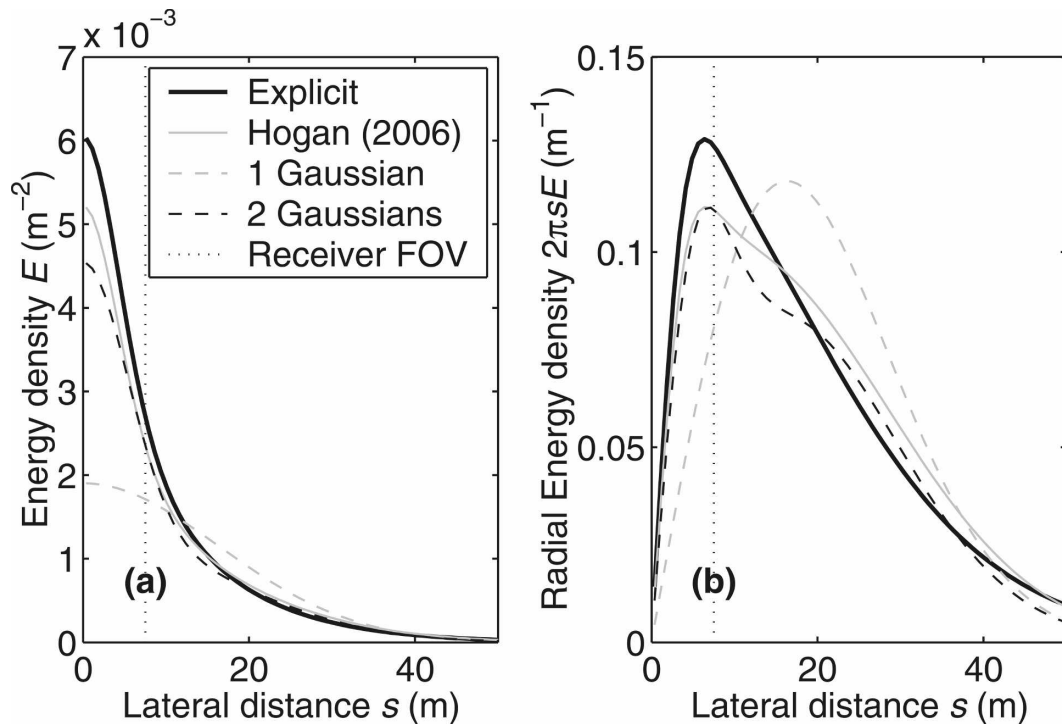


FIG. 3. (a) Lateral distribution of outgoing forward-scattered photon energy (normalized by the transmitted energy) for light that has penetrated to an (equivalent medium) optical depth of 3 in a homogeneous medium with a forward-scattering lobe of width $\Theta = 0.015$. The initial photon distribution has a lateral standard deviation of $\rho_{tr} r = 5$ m. (b) As in (a), but after azimuthal integration (i.e., multiplication by $2\pi s$). The thick black line is from an explicit calculation taken to seventh-order scattering. The remaining solid and dashed lines represent the various approximations discussed in the text. The dotted line at $s = 7.5$ m indicates the receiver field-of-view half-width corresponding to a footprint full width of $X = 15$ m.

backscatter would be to treat all forward-scattered photons as a single Gaussian of energy \hat{P}_a and spatial variance s_a^2 and then estimate these variables from (7) and (8) (i.e., by neglecting \hat{P}_b , s_b^2 , etc). This approach is tested in Fig. 3, which shows the forward-scattered photon distribution calculated “explicitly” for a simple homogeneous cloud, along with several approximations. The explicit calculation considered all possible ways that a multiply scattered photon could arrive at its destination by recursive application of Eqs. (15)–(18) in H06, thereby producing the distribution that is implicitly represented by the E98 method. In this case, E_a and E_b in (6) are the first two of over 8000 Gaussians, representing each of the possible combinations of the 10 range gates in which a photon could be forward scattered.

Because the return journey after backscattering in the equivalent medium is in a vacuum, the apparent backscatter is proportional to the area under the curve in Fig. 3b up to the vertical dotted line, which denotes the half-width of the receiver footprint, $X/2$. It can be seen that the single-Gaussian approximation (the gray

dashed line) does not match the true distribution well, which is distinctly leptokurtic. The disagreement is especially evident for $s < X/2$, indicating that apparent backscatter would be significantly underestimated. This is despite the Gaussian having both the correct energy (i.e., the total area under the curve in Fig. 3b) and variance.

A more sophisticated representation of the photon distribution is clearly needed. The gray solid line in Fig. 3 shows the approximation employed by H06, which used an explicit treatment of double scattering (corresponding to a Gaussian for each of the possible locations at which photons could be forward scattered) but treated all higher-order scatterings by a single Gaussian. The distribution is significantly better represented. It is now shown that almost the same performance can be achieved with only two Gaussians (E_a and E_b), thereby avoiding the nested loop required by H06.

The problem with the single-Gaussian representation is that although its variance s_a^2 is calculated exactly, this variable is often dominated by the contribution of photons that have escaped from the receiver field of view

and contribute nothing to the apparent backscatter. What is required is some way to model just those photons within the field of view. This is achieved by carrying out the procedure described in section 2b twice, the second time with an adjustment after each range gate to ensure that implied width of the single Gaussian E_a does not exceed the receiver footprint width at that height. If it does, then each of the variables is adjusted to remove those photons that were scattered too far outside the field of view. Thus, at half-gate $i + 1/2$, application of (16)–(19) yields the variables describing the full distribution \hat{P} , \bar{s}^2 , $C^{s\xi}$, and $\bar{\zeta}^2$. These are used to calculate the corresponding variables of the single Gaussian (\hat{P}_a , \bar{s}_a^2 , $C_a^{s\xi}$, and $\bar{\zeta}_a^2$) via (7) and (8) but without the b terms. Note that $C^{s\xi}$ and $\bar{\zeta}^2$ are weighted averages, so an expression analogous to (8) may be used. The width of the forward-scattered distribution is then tested to see if it exceeds the half-width of the receiver field of view, $X/2 = \rho_{\text{fov}}r$ (where r is the range to gate $i + 1/2$), and if it does then a scaling factor f is defined:

$$f = \begin{cases} (\rho_{\text{fov}}r)^2/\bar{s}_a^2; & \bar{s}_a^2 < (\rho_{\text{fov}}r)^2, \\ 1; & \bar{s}_a^2 \geq (\rho_{\text{fov}}r)^2. \end{cases} \quad (20)$$

This is then used to scale the variance and total energy as follows:

$$\bar{s}_a^2 \leftarrow f\bar{s}_a^2; \quad (21)$$

$$\hat{P}_a \leftarrow f\hat{P}_a, \quad (22)$$

where (22) ensures that when the variance is reduced, the peak energy (i.e., E_a at $s = 0$) is preserved. The appropriate way to scale $\bar{\zeta}_a^2$ and $C_a^{s\xi}$ is less obvious because these variables depend on the joint distribution of the four variables x , y , ζ_x , and ζ_y , and in particular the x - ζ_x and y - ζ_y correlations (no other correlations exist). In the case that the four variables are normally distributed, it can be shown that

$$C_a^{s\xi} \leftarrow fC_a^{s\xi}, \quad (23)$$

$$\bar{\zeta}_a^2 \leftarrow (f\rho^2 + 1 - \rho^2)\bar{\zeta}_a^2, \quad (24)$$

where the correlation coefficient between position and direction is given by $\rho = C_a^{s\xi}(\bar{s}_a^2 \bar{\zeta}_a^2)^{-1/2}$. Equation (24) has logical limits: in the case that position and direction are uncorrelated ($\rho = 0$), sampling photons by their position has no effect on the variance of their direction, so $\bar{\zeta}_a^2$ is unchanged. Conversely, if they are perfectly correlated, then sampling photons by position has the same fractional effect on $\bar{\zeta}_a^2$ as it does on \bar{s}_a^2 .

After these scalings have been performed at half-gate $i + 1/2$, the variables describing the unscattered distribution are added back on using (7) and (8), and the

procedure in section 2b is repeated to obtain the variables of the full distribution at half-gate $i + 3/2$, and so on. Thus, we obtain a profile of \hat{P}_a and \bar{s}_a^2 describing a single Gaussian whose width is constrained by the receiver field of view. The photons removed from the distribution may still contribute to the backscatter by being forward-scattered back into the receiver field of view. Their energy and width (\hat{P}_b and \bar{s}_b^2) may be calculated from (7) and (8) using the original calculation of \hat{P} and \bar{s}^2 , that is, without the scaling expressed in Eqs. (21)–(24). Thus, we have two Gaussians with which to represent the forward-scattered photon distribution. This is represented by the black dashed line in Fig. 3 and can be seen to be very similar to the H06 distribution up to the receiver half-width. However, the calculations described in this section are $O(N)$ efficient rather than the $O(N^2)$ of the H06 method.

It should be stressed that other methods are possible within the PVC framework. For example, if higher accuracy were required than shown by the approximations in Fig. 3, and $O(N^3)$ efficiency could be tolerated, then a promising approach might be to use the explicit method of E98 for double and triple scattering, but to represent all higher-order scatterings by a single Gaussian using the PVC approach.

d. Calculation of apparent backscatter

The apparent backscatter $\hat{\beta}^d$ can be expressed as the sum of the contributions from single and multiple scattering

$$\hat{\beta}^d = \hat{\beta}_1 + \hat{\beta}_a + \hat{\beta}_b + \dots, \quad (25)$$

where $\hat{\beta}_1 = \beta \exp(-2\delta)$ is the attenuated backscatter due to single scattering (expressed in terms of the true backscatter coefficient β and the optical depth to the point of observation δ) and the remaining terms correspond to the distributions used to describe the forward-scattered photons in section 2. To determine $\hat{\beta}_a$, we need to know the fraction of photons in distribution E_a that are detected by the receiver. In the equivalent medium, the return journey of any backscattered photons is in a vacuum, so the only photons that can be detected by a telescope with a half-angle field of view of ρ_{fov} are those with a lateral distance of $s < \rho_{\text{fov}}r$ (corresponding to the area under the curve to the left of the dotted line in Fig. 3b). Thus we have

$$\hat{\beta}_a = \hat{\beta}_1 F(r) \frac{\int_0^{\rho_{\text{fov}}r} E_a(r,s)s ds}{\int_0^{\rho_{\text{fov}}r} E_u(r,s)s ds}, \quad (26)$$

and similarly for $\hat{\beta}_b$ [and any further terms in Eq. (25)]. In (26), the anisotropic backscatter factor F can be used to account for an anisotropic phase function near 180° , as described in section 3. However, if the phase function is close to isotropic near 180° , then we simply use $F = 1$.

Substitution of the appropriate Gaussian distributions [of the form in Eq. (4)] for both E_u and E_a yields

$$\hat{\beta}_a(r) = \hat{\beta}_1(r)F(r)\hat{P}_a(r) \frac{1 - \exp(-\rho_{\text{fov}}^2 r^2 / s_a^2)}{1 - \exp(-\rho_{\text{fov}}^2 / \rho_{\text{tr}}^2)}, \quad (27)$$

and similarly for $\hat{\beta}_b$. In some cases the lidar receiver operates in the diffraction limit, in which case the receiver pattern would be better described as a Gaussian of $1/e$ half-width ρ_{fov} rather than as the “top-hat” function used above. In this case, one should use

$$\hat{\beta}_a(r) = \hat{\beta}_1(r)F(r)\hat{P}_a(r) \frac{1 + \rho_{\text{tr}}^2 / \rho_{\text{fov}}^2}{1 + s_a^2 / \rho_{\text{fov}}^2 r^2}. \quad (28)$$

See Part II for further details.

In practice, the extinction and true backscatter coefficients will be input on a discrete grid, and care must be taken to ensure that the calculated apparent backscatter is the mean for each layer. This is particularly true if the optical depth of any individual layer is on the same order as or greater than unity because then substantial attenuation occurs within a single layer. We also need to deal with the problem that \hat{P} and s^2 in (27) and (28) were calculated in section 2b at the midpoints between the gates at which extinction and true backscatter are reported. The numerical details of how this is overcome are presented in the appendix.

3. Accounting for anisotropic phase functions near 180°

For singly scattered photons to be detected, they must be scattered through exactly π radians so the backscatter coefficient is sufficient to determine the intensity of the return echo. For small-angle multiple scattering, small-angle forward-scattering events on the outward or return journeys mean that photons scattered in the backward direction by an angle less than π may also be detected by the receiver. Hence, we need to consider the shape of the phase function in the backward direction and the distribution of near- π scattering angles that can result in a photon being detected. This enables the term F in (26) to be estimated.

a. Parameterizing the phase function near 180°

We first consider the scattering by distributions of liquid water droplets. Figure 4 shows the scattering

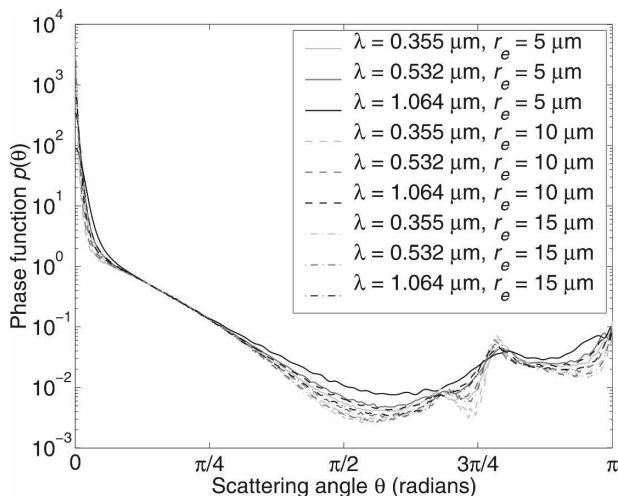


FIG. 4. The scattering phase function of a gamma distribution (of shape parameter 2) of water droplets for three commonly used lidar wavelengths and three values of effective radius (r_e) typical of liquid water clouds. The calculations were performed using Mie theory.

phase function for three common lidar wavelengths and the range of effective radius typically found in stratocumulus (Miles et al. 2000). The phase function can be seen to exhibit a peak in scattering for scattering angles θ close to π , whereas at smaller angles the scattering decreases before reaching a secondary peak corresponding to the “halo” phenomenon. We seek to parameterize the phase function near $\theta = \pi$. Following van de Hulst (1957), the scattering coangle is defined as $\gamma = \pi - \theta$. Figure 5 shows the phase function $p(\theta)$ near $\theta = \pi$, normalized by the value at $\theta = \pi$. Note that the backscatter coefficient (in units of $\text{m}^{-1} \text{sr}^{-1}$) is defined as $\beta = \alpha \tilde{\omega} p(\pi) / 4\pi$, where $\tilde{\omega}$ is the single scattering albedo. The abscissa has also been normalized, using the variable Θ discussed in section 2b. It can be seen that the halo always peaks at $\gamma \approx \Theta$.

The exact shape of the halo depends on the width of the droplet size distribution, which we would not expect to be able to retrieve remotely, so instead we parameterize the shape of the phase function as the sum of a constant and two Gaussians:

$$P(\pi - \gamma) / p(\pi) = U_0 + U_1 \exp[-(V_1 \gamma / \Theta)^2] + U_2 \exp[-(V_2 \gamma / \Theta)^2], \quad (29)$$

where $U_0 = 0.2$, $U_1 = 0.3$, $U_2 = 0.5$, $V_1 = 4.0$, and $V_2 = 0.4$. This is represented in Fig. 5 as the thick dotted line. It can be seen to fit the actual normalized phase functions to within around 30%.

In the case of ice particles, there is some disagreement in the literature regarding the nature of the phase

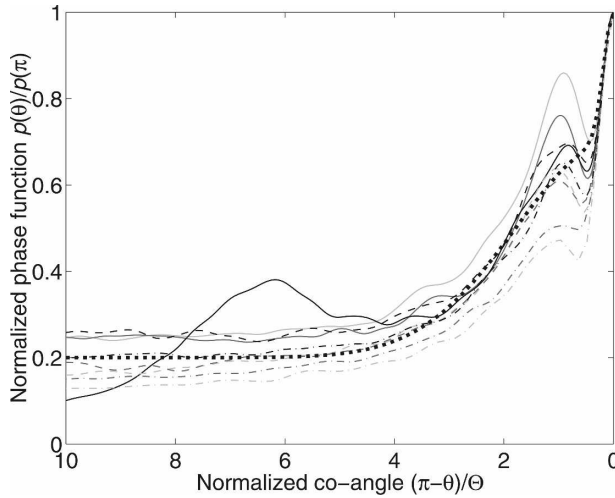


FIG. 5. Droplet-scattering phase function in the vicinity of the backward direction, normalized by the backscatter value $p(\pi)$, vs the scattering coangle normalized by Θ (defined in the text). The thin lines correspond to the same wavelengths and effective radii as in Fig. 4, whereas the large dots correspond to the double-Gaussian fit discussed in section 3a and represented by (29).

function, with observations tending to show much more featureless and flat phase functions than scattering calculations based on idealized ice particle shapes. This is illustrated in Fig. 6: the thin lines show calculations by Yang et al. (2000, hereafter YL00) for three different shapes over a range of sizes, while the thick line shows the smooth phase function fitted to observations by Baran et al. (2001). This discrepancy is likely to be due to the fact that most ice clouds are dominated by irregular aggregates, possibly compounded by factors such as roughened surfaces, aerosol inclusions, and distortions between parallel faces (Baran 2004).

Of principal relevance to this paper is the nature of the phase function near $\theta = \pi$. Here the Baran et al. (2001) phase function is isotropic, which can be explained by the irregular particles lacking the azimuthal symmetry necessary for constructive interference, which is the cause of the peak in the phase function for spheres. By contrast, the YL00 phase functions all exhibit an upturn within 5° of backscatter. Figure 7 shows that when normalized by the value at backscatter, all the YL00 phase functions collapse on to approximately the same curve, which is well fitted by the following expression:

$$p(\pi - \gamma)/p(\pi) = (1 - W) + W \exp(-\gamma/\gamma_0), \quad (30)$$

where $W = 0.89$ and $\gamma_0 = 0.038$. Unlike the near- π peak for liquid droplets shown in Fig. 5 (and indeed the forward lobe for both liquid and ice particles), the peak in the ice phase function apparently shows little depen-

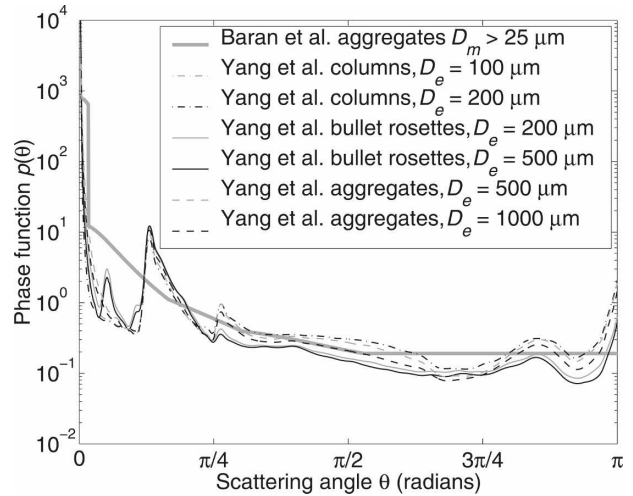


FIG. 6. The scattering phase function at $0.55 \mu\text{m}$ for distributions of ice particles of different habits. The thick gray line corresponds to individual aggregates from Baran et al. (2001); above a maximum dimension (D_m) of $25 \mu\text{m}$ there is no dependence on size, so distributions of such particles would have the same phase function. The remaining lines are from YL00 for gamma distributions of shape parameter 2, with various values of effective diameter (D_e).

dence on particle size or wavelength (via Θ). Its cause is therefore difficult to determine.

b. Calculation of the distribution of photon coangles that contribute to the returned power

Using an approach similar to section 2b, we now calculate the variance of the distribution of the photon

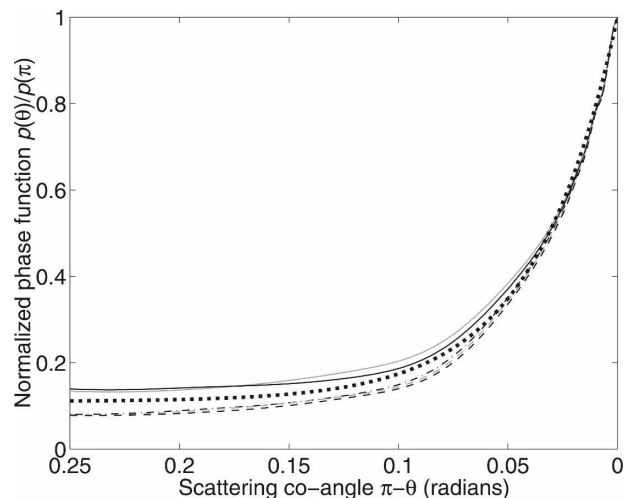


FIG. 7. The YL00 phase functions shown in Fig. 6, but after normalizing by the backscatter value $p(\pi)$ (thin lines). The large dots correspond to the inverse-exponential fit discussed in section 3a and represented by (30).

scattering coangles, weighted by their contribution to the returned power. When coupled to knowledge of the phase function near $\theta = \pi$, such as the parameterization of (29), the F term in (26) may be calculated. Note that because we are considering the equivalent medium, we need only consider forward-scattering events on the outward journey; then, from the position and propagation angle, the scattering coangle that results in a photon returning to the receiver can be determined.

Consider first the component of γ in the x direction, γ_x . From Fig. 2 it can be seen that for a single photon $\gamma_x = \zeta_x - x/r$. Taking the square of both sides and averaging over a distribution of photons yields

$$\overline{\gamma_x^2} = \overline{(\zeta_x - x/r)^2} = \overline{\zeta_x^2} + \overline{x^2/r^2} - 2\overline{x\zeta_x/r}. \quad (31)$$

Noting that the two components of the coangle are related by $\overline{\gamma^2} = \overline{\gamma_x^2} = \overline{\gamma_y^2}$, and similarly for the other quantities, we obtain

$$\overline{\gamma^2} = \overline{\zeta^2} + \overline{s^2/r^2} - 2C^{s\zeta}/r. \quad (32)$$

This operation may be applied to any distribution of photons [e.g., E or E_a in Eq. (6)] to obtain the corresponding variance of the coangle. In practice, it is sufficiently accurate and numerically convenient to calculate $\overline{\gamma^2}$ for the combined distribution $E_a + E_b$, thereby producing one value of F that may be applied in (27) to obtain both $\hat{\beta}_a$ and $\hat{\beta}_b$. Likewise, this value may be applied in other PVC algorithms (e.g., H06).

The variance expressed by (32) includes all photons that have experienced small-angle forward scattering and are returned to the instrument, even if their returning angle is outside the receiver field of view. To select photons within the field of view, a procedure exactly analogous to (24) is applied: if $s^2 > \rho_{\text{fov}}^2 r^2$, then the following scaling is performed:

$$\overline{\gamma^2} \leftarrow \left(\rho^2 \frac{\rho_{\text{fov}}^2 r^2}{s^2} + 1 - \rho^2 \right) \overline{\gamma^2}, \quad (33)$$

where this time ρ is the correlation coefficient between position and scattering coangle; that is, $\rho = C^{s\gamma}(\overline{s^2\overline{\gamma^2}})^{-1/2}$, where the term representing the corresponding covariance is derived in a similar way to (31) and is given by $C^{s\gamma} = C^{s\zeta} - \overline{s^2}/r$.

c. Calculation of anisotropic backscatter factor

The final step in this section is to calculate the backscatter correction factor F . If the normalized phase function in the near- π direction is written as $p(\pi - \gamma)/p(\pi)$ and the distribution of scattering coangles is described by $G(\gamma)$, then we have a convolution:

$$F = 2\pi \int_0^\infty \frac{p(\pi - \gamma)}{p(\pi)} G(\gamma) \gamma d\gamma. \quad (34)$$

It is assumed that the distribution of scattering coangles is described by a Gaussian of the form

$$G(\gamma) = \frac{1}{\pi\gamma^2} \exp\left(-\frac{\gamma^2}{\gamma^2}\right). \quad (35)$$

In the case of liquid water droplets with a near-backscatter phase function approximated by (29), application of (34) yields

$$F = U_0 + \frac{U_1}{1 + \overline{\gamma^2} V_1^2 / \Theta^2} + \frac{U_2}{1 + \overline{\gamma^2} V_2^2 / \Theta^2}, \quad (36)$$

which may be substituted into (27). In the appendix it is described how to cope with the fact that $\overline{\gamma^2}$ is calculated at the half-gates whereas Θ is available at the full gates.

An additional consideration is the contribution from molecular scattering, the phase function of which is isotropic in the backward direction (i.e., $F = 1$). This is incorporated by making F the average of the molecular and particulate contributions, weighted by their respective backscatter coefficients.

In the case of irregular ice particles, the isotropic phase function near $\theta = \pi$ predicted by Baran (2004) implies simply $F = 1$. To apply the YL00 phase functions, we integrate (34) over (30) to yield

$$F_a = (1 - W) + W[1 - g\pi^{1/2} \exp(g^2) \text{erfc}(g)], \quad (37)$$

where $g = (\overline{\gamma^2})^{1/2}/2\gamma_0$ and $\text{erfc}(\cdot)$ denotes the complementary error function. It is important to note that even with the YL00 phase functions, F is close to 1 for most ice clouds. This is because the equivalent-area radius for most ice clouds exceeds $50 \mu\text{m}$, corresponding to a forward-lobe width Θ of typically less than 0.003 rad. After several forward-scattering events, the width of the coangle distribution is only a few times larger than Θ . In Fig. 7 it can be seen that for such small coangles, the phase function is only slightly reduced from its backscatter value.

4. Testing of the algorithm

a. Comparison against other methods

To evaluate the performance of the method, we compare against the model of E98, taken to seventh-order scattering; this model was compared to Monte Carlo calculations in ice cloud by H06 and good agreement was found. A test case is constructed consisting of a liquid cloud from 1 to 1.5 km, with $\alpha = 3 \text{ km}^{-1}$ and $a_G = 10 \mu\text{m}$, and an ice cloud from 3.5 to 6 km, with $\alpha = 0.6 \text{ km}^{-1}$ and $a_G = 50 \mu\text{m}$; hence, both clouds have an optical depth of 1.5. Here, a_G is the equivalent-area

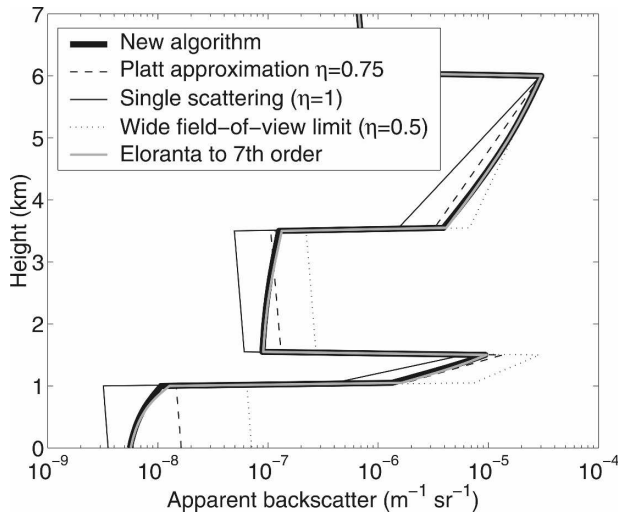


FIG. 8. Comparison of the calculated apparent backscatter for the scenario described in section 4 for a footprint at cloud top of $X = 10$ m.

radius, defined as the radius of a sphere that has the same cross-sectional area as the mean cross-sectional area of the actual size distribution. This scene is observed by a spaceborne 532-nm lidar at an altitude of 700 km. Molecular scattering is assumed to follow an inverse-exponential profile with a scale height of 8 km and a surface backscatter coefficient of $1.6 \times 10^{-6} \text{ m}^{-1} \text{ sr}^{-1}$. All calculations are performed with a vertical resolution of 50 m.

The strength of the multiple scattering depends strongly on the width of the lidar telescope footprint X on the cloud, which varies by several orders of magnitude between ground-based and spaceborne instruments. To fully explore the accuracy of the new method, it has been compared with the E98 model for a wide range of values. The footprint is related to the telescope half-angle ρ_{fov} by $X = 2r\rho_{\text{fov}}$. In each case the laser half-angle beam divergence has been set to $\rho_{\text{tr}} = (2/3)\rho_{\text{fov}}$. Figure 8 shows the results for a footprint of 10 m. The new algorithm agrees with Eloranta's model to within 5% in the ice cloud and to within 10% in the liquid cloud and below, despite being much more efficient.

For comparison, the simpler method of Platt (1973) is shown for an appropriate value of η and the performance is much poorer; in particular, this method is unable to represent the fact that close to the top of the cloud the photons largely stay within the field of view of the receiver, but further down in the profile they progressively escape, particularly in the cloud-free areas. It should be noted that both the new algorithm and the method of Platt (1973) are $O(N)$ efficient. The other

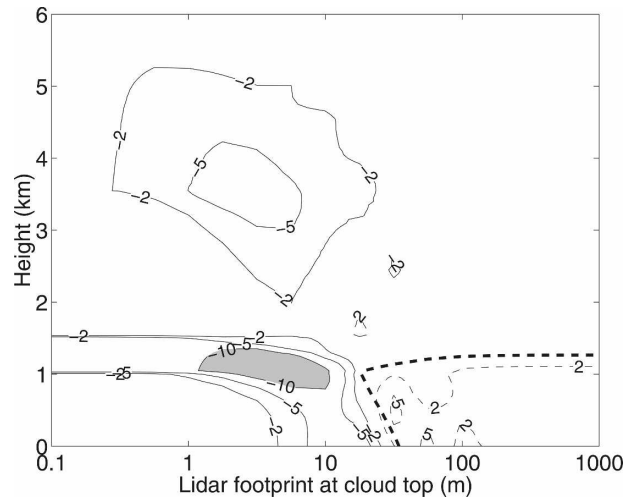


FIG. 9. Percentage difference in apparent backscatter between the new algorithm and the E98 algorithm taken to seventh-order scattering as a function of height and footprint width X . The dashed lines indicate positive values; absolute errors greater than 10% are shaded in gray. The thick dashed line in the bottom right of the image indicates where there is greater than a 5% difference between the sixth and seventh orders of scattering of the E98 model, highlighting that here the E98 model has not fully converged.

lines in Fig. 8 show the two limits within which small-angle calculations must fall: the single-scattering limit equivalent to $\eta = 1$ and the wide field-of-view limit equivalent to $\eta = 0.5$.

To illustrate the behavior over a full range of lidar footprints, Fig. 9 shows the percentage error in the new algorithm with respect to the E98 model taken to seventh order (treated as “truth”). It can be seen that the main error is in the liquid cloud for footprints less than 10 m. This is associated with a tendency to slightly underestimate the peak in the spatial distribution of forward-scattered photons (shown in Fig. 3). For footprints more typical of spaceborne lidars [e.g., 90 m for the Cloud-Aerosol Lidar and Infrared Pathfinder Satellite Observations (CALIPSO) experiment and several hundred meters for the Lidar In-Space Technology Experiment (LITE)], the error is much reduced, implying that this algorithm is well suited to spaceborne lidar.

Figure 10 evaluates the H06 model. The performance is a little better than the new algorithm in all conditions, presumably because double scattering is calculated more accurately. Figure 11 shows how Eloranta's model performs when truncated at fourth-order scattering, typically the highest order that could realistically be incorporated into a retrieval algorithm. It can be seen that substantial errors occur for optically thick liquid water clouds when observed using a footprint typical of a spaceborne lidar.

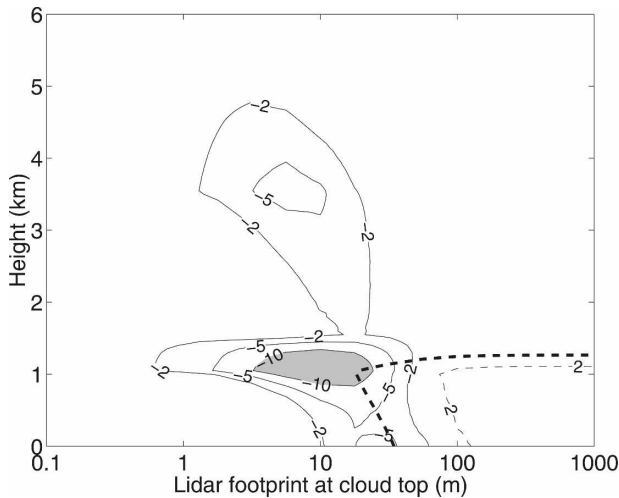


FIG. 10. As Fig. 9, but for the H06 model.

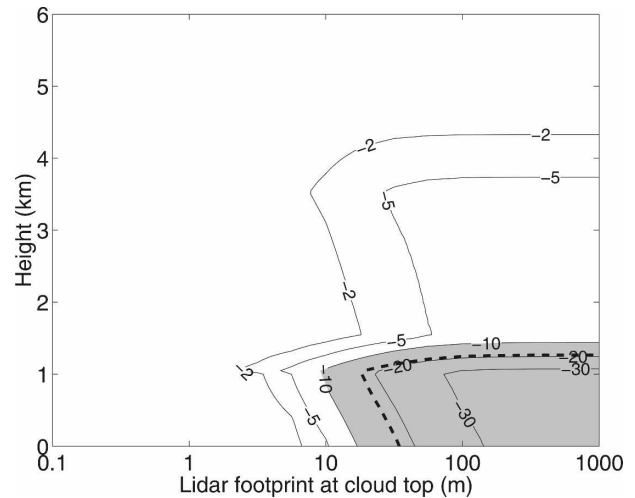


FIG. 11. As Fig. 9, but for the E98 model truncated at fourth-order scattering.

b. The role of the near- 180° phase function and wide-angle scattering

It is useful to know under what conditions it is satisfactory to apply the simple small-angle algorithm and when it is necessary to include the effects of anisotropic phase functions in the backward direction and wide-angle scattering. To determine the effect of the shape of the near- 180° phase function, calculations have been performed for the case shown in Fig. 9 using the new algorithm, adopting the Mie parameterization in the liquid layer [Eqs. (29) and (36)] and the parameterization of the YL00 phase functions [Eqs. (30) and (37)] in the ice layer. Figure 12 shows the results in terms of the error associated with not representing this effect. The difference in the ice cloud is at most around 7%, whereas in the liquid cloud it exceeds 50% for receiver footprints greater than around 20 m. There is no difference in the molecular scattering regions because the shape of the phase function in the backward direction does not affect the way that photons are forward-scattered as they propagate. There are two reasons why one should usually expect smaller differences in real ice clouds than shown in this case. First, the assumed particle radius of $50 \mu\text{m}$ is at the lower end of what is typical of cirrus clouds, and larger particles lead to a narrower forward lobe and hence a smaller scattering coangle and an effective backscatter coefficient more similar to the actual value. Second, as discussed in section 3a, the YL00 phase functions may not be particularly representative of most ice clouds in nature, which have a flatter phase function in the backward direction (Baran 2004).

Figure 13 depicts the error resulting from neglecting the contribution from wide-angle scattering, making

use of the model developed in Part II. For footprints less than 100 m, the only significant error is in the molecular region just beneath cloud base, where pulse stretching of several hundred meters enhances the return. The lack of any significant error within the ice clouds for footprints less than 100 m indicates that ice-cloud retrieval algorithms (e.g., Donovan et al. 2001; Delanoë and Hogan 2008) will be accurate from space with a simple small-angle-only multiple-scattering model that also assumes an isotropic phase function in the backward direction. Nonetheless, if the molecular

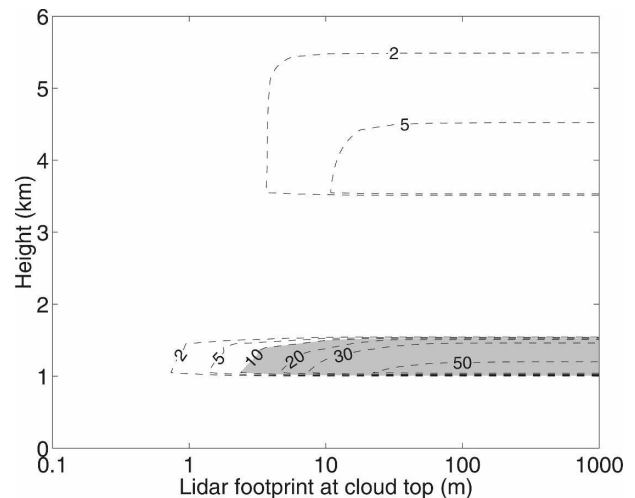


FIG. 12. Percentage error associated with neglecting the shape of the phase function in the near- 180° direction for the case shown in Fig. 9. This was calculated assuming the parameterization of the YL00 phase functions shown in Fig. 7 for the ice cloud and the parameterization of the Mie phase functions shown in Fig. 5 for the liquid cloud.

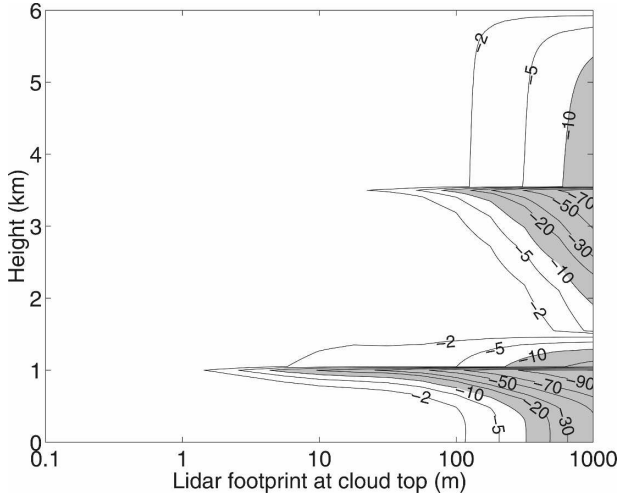


FIG. 13. Percentage error in apparent backscatter between a small-angle-only model and a model that includes both small-angle and wide-angle scattering, for the case shown in Fig. 9. This was calculated using the new model for small-angle scattering and the time-dependent two-stream approximation described in Part II for wide-angle scattering. The liquid cloud was assumed to have an asymmetry factor of 0.85; the ice cloud was assigned a value of 0.7. Both had a single-scattering albedo of unity.

scattering below the cloud is to be used as an optical depth constraint, then care should be taken immediately below cloud where wide-angle scattering is important.

In the case of liquid clouds observed from space, there is a need to include both anisotropic phase functions and wide-angle scattering if the return is to be modeled accurately. It should be stressed that with an optical depth of 1.5, the liquid cloud in this example is less optically thick than most such clouds in reality, for which the error associated with using a small-angle-only model will be much larger. The greater dominance of wide-angle scattering for footprints of several hundred meters is in agreement with the large amount of multiple scattering observed by the LITE lidar (Platt and Winker 1995).

5. Calculation of the Jacobian

In variational retrieval schemes (e.g., Delanoë and Hogan 2008), not only must the forward model provide the apparent backscatter at each gate, it should also provide the Jacobian matrix, consisting of the partial derivatives of apparent backscatter at each gate with respect to the input “state variables” such as extinction coefficient at every gate (i.e., $\partial \hat{\beta}_j^d / \partial \alpha_i$). To fill the elements of an $N \times N$ matrix is clearly at least an $O(N^2)$ process, so this must be done as efficiently as possible if the calculation of the Jacobian is to be commensurate

in speed with the $O(N)$ efficiency of the main algorithm. An approximate Jacobian may be calculated by making use of the Platt (1973) expression [Eq. (3)]. First we rewrite (3) in a simple discrete form and in terms of the natural logarithm of backscatter:

$$\ln \hat{\beta}_j^d = \ln \beta_j - 2\eta_j \delta_{j-1/2} \quad (38)$$

$$= \ln \beta_j - 2\eta_j \sum_{i=1}^{j-1} \alpha_i \Delta r_i. \quad (39)$$

Equation (38) is used to calculate η at each gate as a function of variables calculated within the algorithm: $\eta_j = \ln(\beta_j / \hat{\beta}_j^d) / (2\delta_{j-1/2})$. Making the approximation that $\partial \eta_j / \partial \alpha_i = 0$, the Jacobian can be calculated from (39) to obtain

$$\frac{\partial \ln \hat{\beta}_j^d}{\partial \alpha_i} = -2\eta_j \Delta r_i \quad (40)$$

for $i < j$, and $\partial \ln \hat{\beta}_j^d / \partial \alpha_i = 0$ otherwise.

6. Conclusions

This paper has presented a fast model for calculating the multiply scattered lidar returns from clouds in the small-angle regime. It is shown to be one of a family of possible methods based on the photon variance-covariance (PVC) modeling approach, which includes the method of H06. It is applicable to ice-cloud observations by both ground-based and satellite lidar provided that the receiver footprint is less than around 100 m. For larger footprints or for observations of liquid clouds, it should be supplemented by the wide-angle scattering model presented in Part II. Benchmark calculations have been performed and the execution time is found to be proportional to N and on the order of 10^{-4} s for a profile composed of $N = 100$ points (on a 1-GHz Intel processor). It is therefore suitable for direct application as the “forward model” in combined radar-lidar observations of ice clouds from space (e.g., Donovan et al. 2001; Delanoë and Hogan 2008), where execution time is critical because of the high rate at which data are being recorded. See Part II for a comparison of the speeds of various techniques.

A difficulty in the past has been how to rigorously account for anisotropic phase functions in the near- 180° direction. Here it has been shown that by parameterizing the phase function of droplets and idealized ice particles near 180° , and by careful modeling of the variance of the scattering coangle in large-angle scattering events, this effect can be accounted for. In liquid clouds it is found to reduce the apparent backscatter by up to 50%. In ice clouds composed of pristine crystals the effect is much less, but in any case observations suggest

that most cirrus clouds are dominated by irregular particles for which the phase function is nearly isotropic in the vicinity of 180° (Baran 2004).

Acknowledgments. I am grateful to Ulla Wandinger and Anthony Baran for useful discussions on the nature of ice particle phase functions, and to Alessandro Battaglia for valuable comments on the original manuscript.

APPENDIX

Numerical Implementation

In sections 2d and 3c the problem of the variables not being on the same grid was highlighted. Specifically, the input properties of the cloud such as Θ and the unattenuated backscatter β are available on one grid, whereas \bar{s}^2 and $\bar{\gamma}^2$ are calculated at the midpoints of this grid, making it difficult to apply (27) and (28). For the most accurate estimate of apparent backscatter, especially on coarse grids for which significant attenuation occurs within one range gate, we define $\hat{\beta}_i^d$ as the mean apparent backscatter between ranges $r_{i-1/2}$ and $r_{i+1/2}$ (over which the extinction coefficient α_i and true backscatter coefficient β_i are constant) as follows:

$$\hat{\beta}_i^d = \frac{1}{\Delta r_i} \int_{r_{i-1/2}}^{r_{i+1/2}} \hat{\beta}^d(r) dr, \quad (\text{A1})$$

where $\Delta r = r_{i+1/2} - r_{i-1/2}$. It is convenient to define a “multiple scattering factor” as

$$M = 1 + F \times (\hat{\beta}_a + \hat{\beta}_b) / \hat{\beta}_1, \quad (\text{A2})$$

such that (25) becomes simply $\hat{\beta}_i^d = M\hat{\beta}_1$. To determine $\hat{\beta}_i^d$, we first calculate the multiple scattering factor at the neighboring half-gates ($M_{i-1/2}$ and $M_{i+1/2}$) because it is only dependent itself on variables at half-gates. The exception is Θ in (36) which is taken at gate i for calculating F at both half-gates.

High-resolution runs of the algorithm have revealed that in most cases it is a reasonable assumption to assume that M varies exponentially between two half-gates; that is, $M(r) = M_{i-1/2}^{1-r'} M_{i+1/2}^{r'}$, where $r' = (r - r_{i-1/2})/\Delta r_i$ is the normalized distance between half-gates $i - 1/2$ and $i + 1/2$. Noting that we may also write $\hat{\beta}_1(r') = \beta_i \exp[-2(\delta_{i-1/2} + \alpha_i \Delta r_i r')]$, (A1) becomes

$$\hat{\beta}_i^d = \frac{\beta_i \exp(-2\delta_{i-1/2})}{\Delta r_i} \times \int_0^1 \exp\left[\left(\ln \frac{M_{i+1/2}}{M_{i-1/2}} - 2\alpha_i \Delta r_i\right)r'\right] dr', \quad (\text{A3})$$

which yields

$$\hat{\beta}_i^d = \beta_i \exp(-2\delta_{i-1/2}) \frac{M_{i-1/2} - M_{i+1/2} \exp(-2\alpha_i \Delta r_i)}{2\alpha_i \Delta r_i - \ln(M_{i+1/2}/M_{i-1/2})}. \quad (\text{A4})$$

This is straightforward to calculate at each gate.

REFERENCES

- Ackerman, T. P., and G. M. Stokes, 2003: The Atmospheric Radiation Measurement Program. *Phys. Today*, **56**, 38–44.
- Baran, A. J., 2004: On the scattering and absorption properties of cirrus cloud. *J. Quant. Spectrosc. Radiat. Transfer*, **89**, 17–36.
- , P. N. Francis, L.-C. Labonnote, and M. Doutriaux-Boucher, 2001: A scattering phase function for ice clouds: Tests of applicability using aircraft and satellite multi-angle multi-wavelength radiance measurements of cirrus. *Quart. J. Roy. Meteor. Soc.*, **127**, 2395–2416.
- Battaglia, A., M. O. Ajewole, and C. Simmer, 2007: Evaluation of radar multiple scattering effects in CloudSat configuration. *Atmos. Chem. Phys.*, **7**, 1719–1730.
- Bissonnette, L. R., 2005: Lidar and multiple scattering. *Lidar Range-Resolved Optical Remote Sensing of the Atmosphere*, C. Weitkamp, Ed., Springer, 43–104.
- Delanoë, J., and R. J. Hogan, 2008: A variational method for retrieving ice cloud properties from combined radar, lidar, and infrared radiometer. *J. Geophys. Res.*, **113**, D07204, doi:10.1029/2007JD009000.
- Donovan, D. P., and Coauthors, 2001: Cloud effective particle size and water content profile retrievals using combined lidar and radar observations. 2. Comparison with IR radiometer and in situ measurements of ice clouds. *J. Geophys. Res.*, **106**, 27 449–27 464.
- Eloranta, E. W., 1998: A practical model for the calculation of multiply scattered lidar returns. *Appl. Opt.*, **37**, 2464–2472.
- Hogan, R. J., 2006: Fast approximate calculation of multiply scattered lidar returns. *Appl. Opt.*, **45**, 5984–5992.
- , and A. Battaglia, 2008: Fast lidar and radar multiple-scattering models. Part II: Wide-angle scattering using the time-dependent two-stream approximation. *J. Atmos. Sci.*, **65**, 3636–3651.
- , D. P. Donovan, C. Tinel, M. E. Brooks, D. Bouniol, A. J. Illingworth, and J. P. V. Póiares Baptista, 2006: Independent evaluation of the ability of spaceborne radar and lidar to retrieve the microphysical and radiative properties of ice clouds. *J. Atmos. Oceanic Technol.*, **23**, 211–227.
- Illingworth, A. J., and Coauthors, 2007: Cloudnet—Continuous evaluation of cloud profiles in seven operational models using ground-based observations. *Bull. Amer. Meteor. Soc.*, **88**, 883–898.
- Katsev, I. L., E. P. Zege, A. S. Prikhach, and I. N. Polonsky, 1997: Efficient technique to determine backscattered light power for various atmospheric and oceanic sounding and imaging systems. *J. Opt. Soc. Amer.*, **14A**, 1338–1346.
- Miles, N. L., J. Verlinde, and E. E. Clothiaux, 2000: Cloud droplet size distributions in low-level stratiform clouds. *J. Atmos. Sci.*, **57**, 295–311.
- Nicolas, F., L. R. Bissonnette, and P. H. Flamant, 1997: Lidar effective multiple-scattering coefficients in cirrus clouds. *Appl. Opt.*, **36**, 3458–3468.
- Platt, C. M. R., 1973: Lidar and radiometric observations of cirrus clouds. *J. Atmos. Sci.*, **30**, 1191–1204.

- , and D. M. Winker, 1995: Multiple scattering effects in clouds observed from LITE. *Optics in Atmospheric Propagation and Adaptive Systems*, A. Kohnle, Ed., International Society for Optical Engineering (SPIE Proceedings, Vol. 2580), 60–71.
- Stephens, G. L., and Coauthors, 2002: The CloudSat Mission and the A-Train. *Bull. Amer. Meteor. Soc.*, **83**, 1771–1790.
- Tinel, C., J. Testud, J. Pelon, R. J. Hogan, A. Protat, J. Delanoë, and D. Bouniol, 2005: The retrieval of ice cloud properties from cloud radar and lidar synergy. *J. Appl. Meteor.*, **44**, 860–875.
- Van de Hulst, H. D., 1957: *Light Scattering by Small Particles*. Wiley, 470 pp.
- Winker, D. M., J. Pelon, and M. P. McCormick, 2003: The CALIPSO mission: Spaceborne lidar for observation of aerosols and clouds. *Lidar Remote Sensing for Industry and Environment Monitoring III*, U. N. Singh, T. Itabe, and Z. Liu, Eds., International Society for Optical Engineering (SPIE Proceedings, Vol. 4893), 1–11.
- Yang, P., K. N. Liou, K. Wyser, and D. Mitchell, 2000: Parameterization of the scattering and absorption properties of individual ice crystals. *J. Geophys. Res.*, **105**, 4699–4718.